remote sensing

MDPI

Article

Coastal Storm-Induced Sinkholes: Insights from Unmanned Aerial Vehicle Monitoring

Alice Busetti, Christian Leone, Amerigo Corradetti, Saverio Fracaros, Sebastian Spadotto, Pietro Rai, Luca Zini and Chiara Calligaris *

Department of Mathematics, Informatics and Geosciences, University of Trieste, 34127 Trieste, Italy; abusetti@units.it (A.B.); christian.leone@units.it (C.L.); amerigo.corradetti@units.it (A.C.); saverio.fracaros@phd.units.it (S.F.); sebastian.spadotto@phd.units.it (S.S.); pietro.rai@phd.units.it (P.R.); zini@units.it (L.Z.)

* Correspondence: calligar@units.it

Abstract: In recent decades, the scientific community has increasingly focused on extreme events linked to climate change, which are leading to more intense and frequent natural disasters. The Mediterranean can be considered a hotspot where the effects of these changes are expected to be more intense compared to other regions of the planet. Italy is not exempt; in fact, with its extensive shoreline, it is particularly vulnerable, especially to high sea levels and coastal erosions. In this framework, from late October to early November 2023, six storm surges occurred in the Gulf of Trieste (NE Italy). These events, characterized by winds from 190°N to 220°N and the significant wave height, which reached up to 1.81 m nearshore—an uncommon meteorological condition in the northern Adriatic Sea—caused the occurrence of eight coastal sinkholes and substantial damages to man-made structures. Thanks to Unmanned Aerial Vehicles (UAVs) and their derived products (high-resolution orthomosaics, Digital Elevation Models—DEMs, and point clouds), it was possible to study these features over time, enabling long-term coastal dynamics monitoring, which can be crucial for timely and effective response and restoration efforts.

Keywords: coastal sinkholes; climate changes; UAV monitoring; high-resolution orthomosaics; DEMs; point clouds; wave modelling; geological hazard; Italy

Citation: Busetti, A.; Leone, C.; Corradetti, A.; Fracaros, S.; Spadotto, S.; Rai, P.; Zini, L.; Calligaris, C. Coastal Storm-Induced Sinkholes: Insights from Unmanned Aerial Vehicle Monitoring. *Remote Sens.* **2024**, *16*, 3681. https://doi.org/10.3390/rs16193681

Academic Editor: Paraskevas Tsangaratos

Received: 29 August 2024
Revised: 26 September 2024
Accepted: 28 September 2024
Published: 2 October 2024

1. Introduction

The First Report on the Climate and Environmental Change Assessment (MedECC) [1] highlights that the Mediterranean is warming 20% faster than the global average [2–4], affecting both terrestrial and marine environments. This makes it a hotspot [5] where the effects of climate change are expected to be more intense compared to other regions of the planet [6,7]. Within this context, scientists unanimously agree that coastal areas are among the most impacted: even a small increase in sea level can have devastating effects on coastal habitats [4,8,9], leading to the loss of sandy shores and causing damage to settlements, infrastructure, and ecosystems [10–13].

In recent years, the Mediterranean basin has experienced an increase in both the intensity and frequency of coastal flooding events [14–16]. Therefore, direct impacts generated by storms hold significant social and scientific interest within this area [17–23]. This interest is not solely due to sea level rise [24]; it is also correlated with the growing population, considering that about 75% of the Mediterranean inhabitants are concentrated along coastal areas [25], and this percentage is expected to increase further in the future [10,26]. However, the critical issues are not only limited to low-lying coasts. Rising sea levels and wave activity could also exacerbate erosive phenomena even on typically high, rocky coasts [27]. In this regard, a possible effect of storm surges is a worldwide little-known phenomenon called coastal sinkholes [28,29]. Sinkholes are closed, depressed landforms that can form suddenly due to a collapse or which can have a lower development as in the

suffosion processes or in the dissolution ones [28]. These features (intended as subsidence sinkholes—*sensu* [28]) can significantly affect the geomorphological evolution of coastlines by controlling the formation and preferential orientation of bays and inlets as observed in the Apulia region (SE Italy) and Malta Island [30–40]. Despite their importance, these phenomena have caught little interest in the scientific community while they generally become trending topics in local news (Table 1 and Figure 1).

Table 1. Recent coastal sinkholes occurred around the world and appeared on the news.

Location	Date	Dimension	Causes	References
Scotland	4 February 2021	Diameter: 3 m	storm	[41]
Scotland	30 October 2023	Diameter: 5 m	storm	[42]
England	7 October 2019	Axis: 2.4 × 6 m Depth: 2.4 m	very heavy rainfall combined with the highest tide of the year	[43]
England	10 January 2022	Diameter: 12 m	coastal erosion	[44]
Australia	10 June 2021		ongoing coastal erosion	[45]
Oregon (USA)	22 January 2023	Diameter: 6 m Depth: 4.5 m	coastal erosion	[46]
Oregon (USA)	8 May 2023	Diameter: 3 m	coastal erosion	[47]
Italy (Otranto)			progressive erosion by sea wave action	[28]
Italy (Sicily)	11 December 2021		coastal erosion	[48]
Italy (Sicily)	28 November 2023		floods	[49]
Italy (Naples)	November 2023		persistent rainfall and high tide	[50]

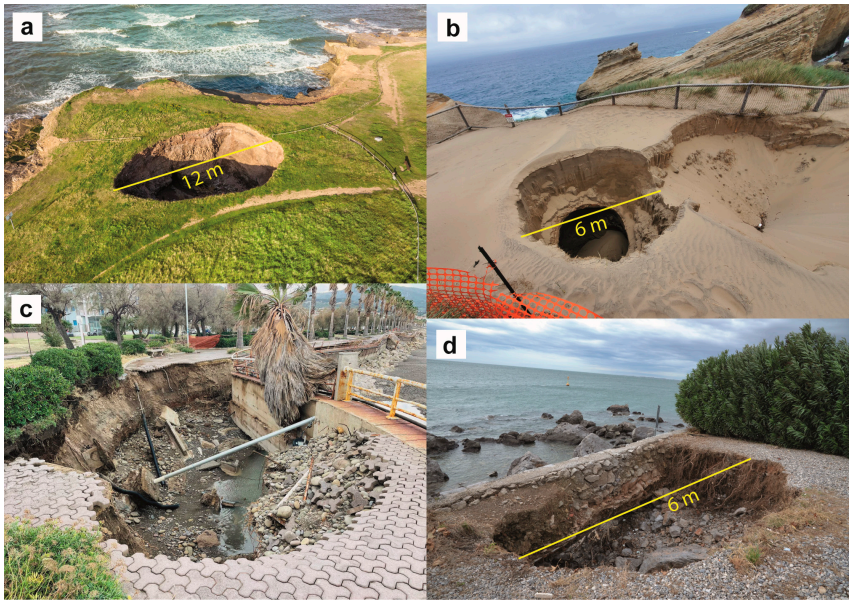

Figure 1. Recent coastal sinkhole worldwide: (**a**) Aerial view of Souter sinkhole and surrounding coastal landscape in Sunderland, England (photo credits: National Trust Images/Annapurna Mellor, Souter Lighthouse and The Leas, Tyne and Wear); (**b**) Sinkhole formed on January 2023 in Cape Kiwanda State Park, Oregon (photo credits: Oregon Parks and Recreation Department Media Hub); (**c**) Sinkhole due to a storm surge event on November 2023 in Sant'Agata di Militello (Sicily, Italy) (photo credits: "In Alto Mare-Sant'Agata di Militello" [49]; (**d**) Sinkhole formed at the Sistiana Bay (Friuli Venezia Giulia, Italy) after a storm surge on October 2023 (photo credits: Busetti A).

The occurrence and evolution of sinkholes, typically associated with inland environments due to the presence of carbonates and evaporites ([28,51–56], and all the references within), can be monitored through the use of tools such as Unmanned Aerial Vehicles (UAVs). UAVs facilitate frequent, rapid, accurate, and low-cost surveying [57,58]. UAVs

and particularly the digital photogrammetry technique relying on the well-known Structure from Motion-Multi View Stereo (SfM-MVS) photogrammetry workflow [59] have been used to produce terrain models for predictive purposes (e.g., [60–62]) and to conduct post-event assessments (e.g., [63]). These technologies were also employed to monitor the impact of extreme events on anthropized areas (e.g., [64]) and, particularly, have recently been used for surveys (e.g., [65–69]) and the assessment of erosive effects and post-event morphological impacts (Rapid Environmental Assessment—REA) on low coasts [70,71]. Despite this broad application of UAVs in various contexts, to the authors' knowledge, UAVs have never been used to investigate storm-induced coastal sinkholes and their evolution, as proposed in the present paper. This study focused on the Northern Adriatic Sea (the NE of the Mediterranean Sea) and specifically on the Gulf of Trieste (Figure 2), which experienced significant meteorological and marine phenomena along high and urbanized coasts, such as the event that occurred in November 1969 [72]. More recently, in late October and early November 2023, a similar event occurred in the same areas, severely affecting the localities of Sistiana Mare and Barcola. This event resulted in substantial damage to infrastructure, buildings, and beach facilities, as well as the formation of several coastal sinkholes. To assess the evolution of the latter, high-resolution (HR) orthomosaics, Digital Elevation Models (DEMs), and point clouds were created from UAV imagery and compared. Several UAV surveys were carried out between September 2023 and February 2024. Furthermore, for the sake of data reproducibility and future comparisons, as well as to better document the phenomena, three additional 3D models of the storm-induced sinkholes were produced.

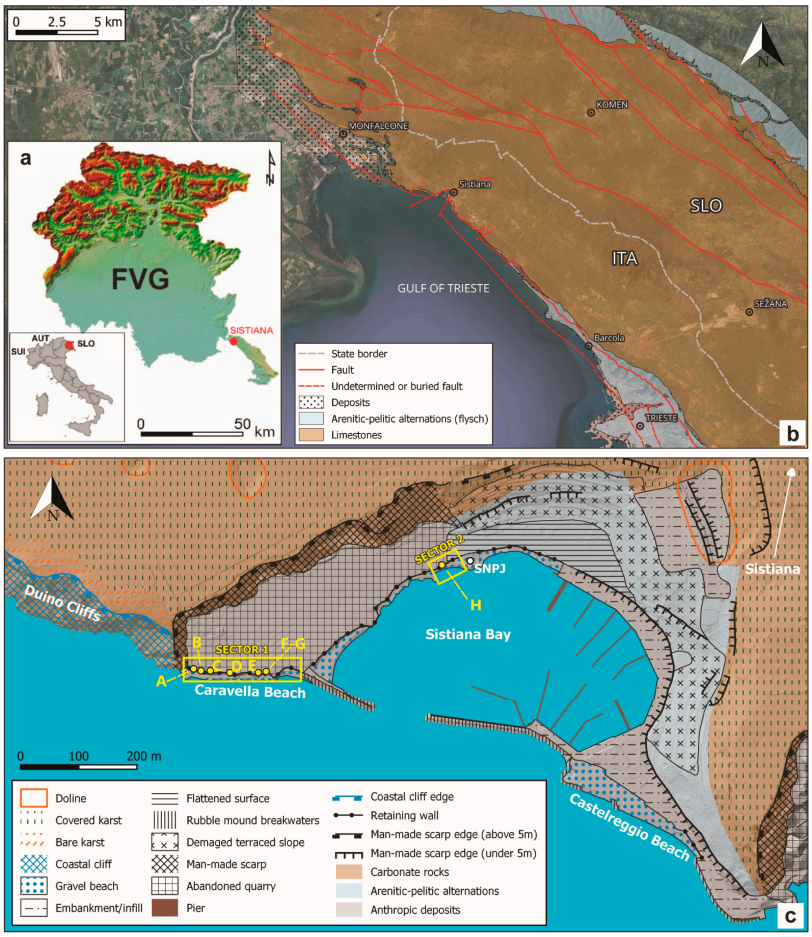

Figure 2. Study area location: (**a**) Friuli Venezia Giulia (FVG) region; (**b**) simplified lithological map of part of the Classical Karst Region; (**c**) geomorphological map of the study area. Yellow rectangles identify SECTOR 1 and SECTOR 2, and the letters are related to the occurred sinkholes.

Finally, to simulate the intensity of waves in the study area, wave motion modeling related to the storm events of autumn 2023 was conducted. This approach enabled the study of the correlation between the characteristics of the storm events in terms of wave parameters and their direct effects on the Sistiana Mare coastline.

2. Study Area

Sistiana Mare is located in the western sector of the Gulf of Trieste (Friuli Venezia Giulia Region, NE Italy), which is in the northernmost part of the Adriatic Sea (Figure 2a). The area is part of the Classical Karst Region, a carbonate plateau (approximately 750 km^2) shared between Italy and Slovenia (Figure 2b). The region is renowned worldwide for its abundance and variety of epigean and hypogean karst landforms [73]. From a geological point of view, this carbonate plateau belongs to the northwestern sector of the External Dinarides (e.g., [74]), a fold-and-thrust belt formed during the NE-SW-oriented Jurassic-Eocene convergence between the European and Adria-related units [75–77]. The plateau is characterized by an SW-verging asymmetrical anticline affecting Mesozoic to lower Eocene shallow-water carbonates. As a result of the convergence, during Eocene times, these shallow-water carbonates were subjected to drowning—marked by the deposition of a siliciclastic unit—caused by the accelerating flexural subsidence related to the development of the Dinaric fold-and-thrust belt and foreland basin system (e.g., [74,78–80]). Geomorphologically, the area is defined as a mature karst, as evidenced by the abundance of karst features such as more than 4000 caves and over 32,800 dolines, which give the topographical surface an irregular and rough appearance [81].

The study area is characterized by distinctive morphologies linked not only to the main structural characteristic of the Classical Karst Region but also to the anthropogenic modifications that occurred over time. On the westernmost side of the area, the shoreline is a limestone-plunging cliff towering 70 m high [82] known as the Duino Cliffs [72], characterized by steeply dipping to overturned stratification [82] belonging to the frontal flank of the karst anticline (Figure 2b,c). Moving southeastward, the area is characterized by a disused quarry that was converted into an urbanized area, which includes beach facilities such as Caravella Beach, a small sewage treatment plant, and a tourist area partially occupied by a parking place. Between the two rubble mound breakwaters lies Sistiana Bay, a fully anthropized area featuring gravel beaches, sailing clubs, a small harbor, asphalted parking areas, and spaces for recreational activities. At the extreme southeastern side of the bay, beyond the breakwater, Castelreggio Beach is sited. The stretches of coastline considered for the present study are the gravel beach of Caravella (SECTOR 1) and the western sector of the Sistiana Bay up to the Pietas Julia sailing club (SNPJ) (SECTOR 2) (Figure 2). In the entire area described above, immediately upstream of the beaches and separating them from the man-made plain areas, a stone retaining wall, 1 to 3 m high, is present.

Physiographically, the Gulf of Trieste is a shallow basin with a mean depth of 16.2 m and a maximum depth of 32.6 m [83]. The shoreface has steeper slopes in the southeast and gentler slopes in the northern sector, where the 20 m isobath extends up to 8 km away from the coastline (Figure 3). Additionally, the Gulf is characterized by bathymetric highs, such as the Mula Muggia sandbank (Figure 3) [84–86] and the seabed rocky outcrops of Trezza Grande and Trezza Piccola [86,87], located in the northern part of the Gulf. Bathymetric lows, such as the depression of Cape Madona just north of Piran [82], are also present. This bathymetric variability can influence wave height depending on the wind direction. Sistiana Mare is exposed only to the southwest winds at angles between 200 and 220 degrees, where the fetch exceeds 100 km. In all the other directions, the fetch is limited below 30 km (Figure 3).

Based on data recorded by three buoys (DWRG1, DWRG3, and Paloma), several considerations were made on the wave and wind characteristics in this area.

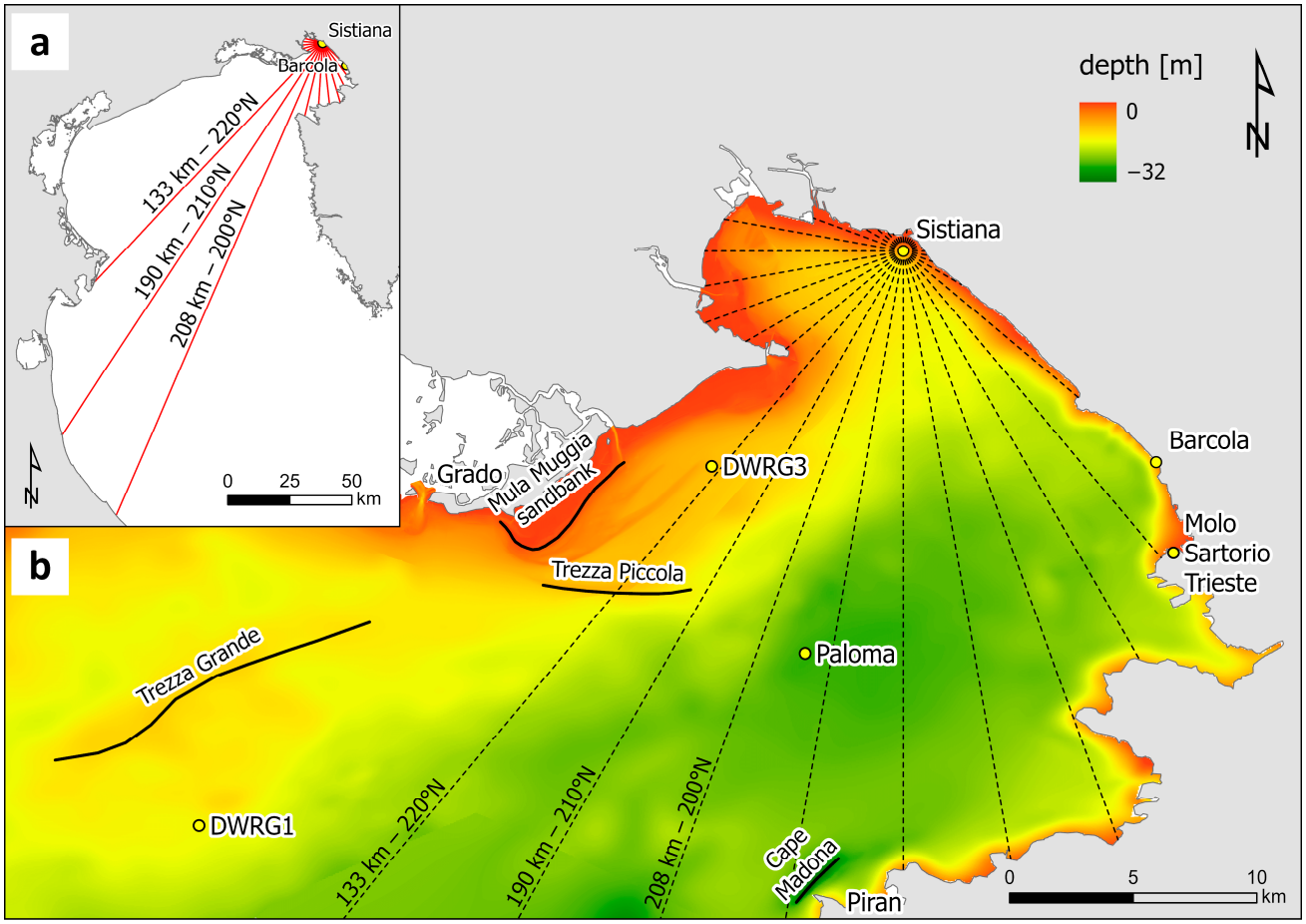

Figure 3. (**a**) Fetch referred to the study area and (**b**) bathymetric model of the Gulf of Trieste and monitoring system locations: DWRG1 (13.24°E, 45.56°N, 15.2 m depth) and DWRG3 (13.52°E, 45.69°N, 9.7 m depth) wave buoys, Paloma station (13.57°E, 45.62°N, 10 m height), and Molo Sartorio (Trieste) tide gauge (13.76°E, 45.65°N). DWRG1 and DWRG3 (installed and managed by Istituto Nazionale di Oceanografia e di Geofisica Sperimentale (OGS), record semi-hourly data; Paloma (Italian acronyms of Advanced Platform Oceanographic Laboratory Adriatic Sea), installed 8 nautical miles off the coast of Trieste between Piran (Slovenia) and Grado, measure both wind speed and direction with a sampling rate of 15 min. The bathymetric model was obtained from one of the European Marine Observation and Data Network (EMODnet) of 2022 [88] integrated with the bathymetry provided by [89] and higher resolution bathymetry of the northern coastal area.

The Gulf usually experiences anticlockwise semi-diurnal tides with a mean range of 76 cm [90]. Spring tides average about 105 cm, while neap tides average about 22 cm [91]. Based on data collected at the DWRG1 buoy (Figure 3), NE and SE winds generate a bimodal wave regime (Figure 4a), with a mean significant wave height (Hs) of less than 0.5 m. Events with Hs greater than 0.5 m account for 25.2% of the overall record, with prevailing waves from the SSE (10.7%) and ENE (10.5%). The highest wave heights, reaching up to 4.4 m, are associated with SE-wind due to its longer fetch with respect to the buoy [92]. The wave buoy DWRG3 (Figure 3), closer to the study area, recorded only 11.5% of events with Hs greater than 0.5 m, originating from two main directions. However, data from both buoys indicate that waves recorded at DWRG3 (Figure 4b) are rotated clockwise with respect to those at DWRG1 (Figure 4a).

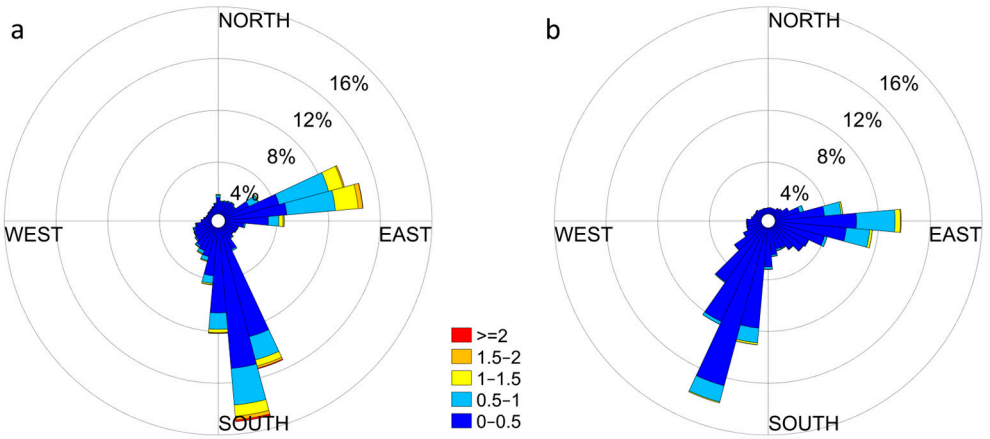

Figure 4. Wave roses of (**a**) DWRG1 relating to the time interval 2004–2023, and (**b**) DWRG3 relating to the time interval 2007–2023.

3. The Extreme Storm Events

From the local news [93], it emerges that severe storms, accompanied by significant damages, occurred in the past in the study area (Figure 5). Historical chronicles report events such as that of June 14, 1911, another in 1969, and a more recent one in 1984. All of them had a violent impact on the Trieste waterfront. Similarly to these past events, between October and November 2023, a new period of bad weather characterized by multiple storm events impacted the Barcola waterfront and Sistiana Mare (a coastline of approximately 4.5 km). The estimated damages, including those associated with the occurrence of several coastal sinkholes, amounted to millions of euros (Figure 5) [94]. Based on wind recordings from the Paloma weather station and wave recordings from the DWRG1 buoy, six different storm events were identified (Table 2). Unluckily, the DWRG3 buoy ceased functioning shortly before the series of storm events and was therefore not considered.

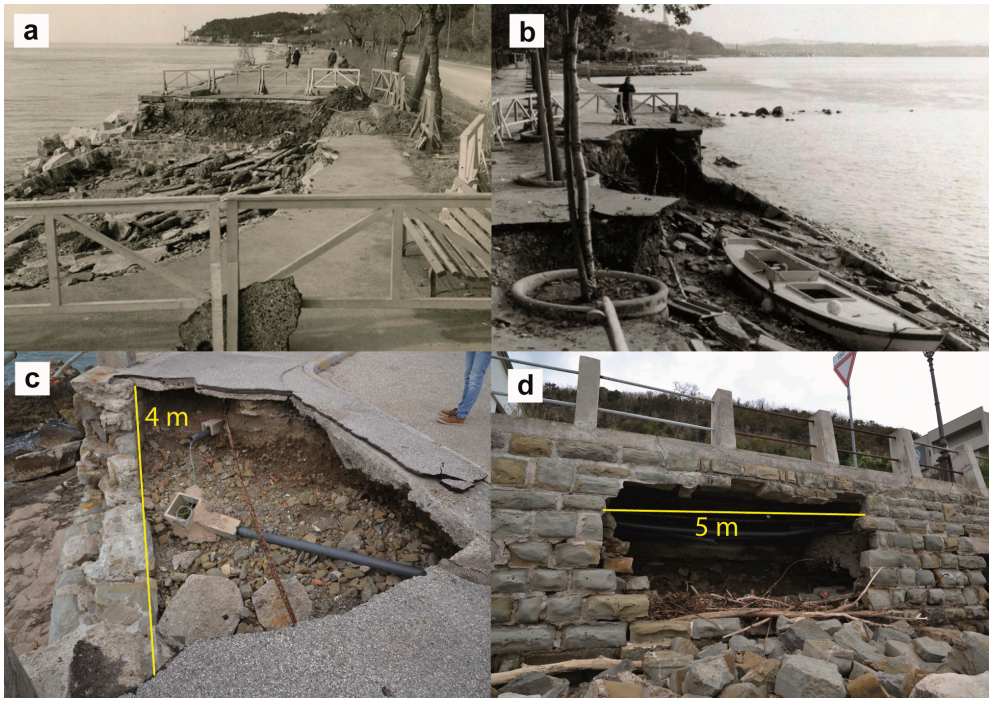

Figure 5. Historical (**a**,**b**) and recent (**c**,**d**) images of the damages that occurred along Barcola waterfront (a and b, photo credits: ASTS, Commissariato del Governo nella Regione Friuli Venezia Giulia, Fototeca (b. 1, ex b. 8, in riordinamento) [72]; c and d, photo credits: Busetti A).

Table 2. Storm events: meteo-marine characteristics.

Storm Event	Storm Date	Hs (Direction) at DWRG1 [m]	Wind Speed (Direction) at Paloma [m/s]
EVENT 1	27 October 2023 06:00	2.26 (170°N)	15.0 (220°N)
EVENT 2	30 October 2023 20:30	2.28 (166°N)	12.2 (179°N)
EVENT 3	31 October 2023 13:00	2.07 (205°N)	13.9 (265°N)
EVENT 4	2 November 2023 17:30	3.24 (175°N)	12.2 (187°N)
EVENT 5	3 November 2023 14:00	2.72 (197°N)	18.3 (221°N)
EVENT 6	5 November 2023 03:00	3.77 (172°N)	14.7 (235°N)

4. Materials and Methods

To calculate the intensity of surge events on the Sistiana Mare coastline and to correlate the evolution of the observed sinkholes with the storm events, wave modeling was performed using MIKE 21. In addition, the evolution of sinkholes along the Sistiana Mare coastline was assessed by creating and comparing High Resolution (HR) 3D models, orthomosaics, and DEMs. These data products were created by applying an SfM-MVS photogrammetry processing workflow to six sets of UAV images acquired between 29 September 2023 and 13 February 2024. Furthermore, to better define the geometry and characteristics of four storm-induced landforms among the largest observed, three additional small-scale and higher-resolution 3D models were produced. A lower-resolution version of these models has been made available in the Sketchfab 3D model public repository (see Section 5.3. HR 3D Models) for documentation and accessibility purposes.

4.1. Wave Modelling

Modelling is a widely used tool to study coastal dynamics [95–99], serving as a knowledge base for both morphodynamic interpretations and engineering purposes of designing coastal works. The lack of wave buoys near the study area necessitated wave modeling to accurately represent the wave motion impacting the Gulf of Trieste. The spectral wave module of the model MIKE 21 by ©DHI was used to simulate the spatial distribution of the wave parameters (significant wave height, mean wave direction, peak wave period, and wave power) during the extreme storm events of autumn 2023.

Spatial discretization was carried out using the finite volume approach applied to unstructured meshes. The mesh was divided into 3 zones with different resolutions: an offshore zone generated starting from a vertex spacing of 675 m on the edge, a central zone built from a spacing of 225 m, and an area near the coast where the spacing between the vertices was 75 m. The resulting mesh has a total of 40,992 nodes and 81,128 elements. Four boundaries were defined: the northern Adriatic boundary towards the southwest, a closed boundary representing the shoreline, and two lateral boundaries connecting the closed and the Adriatic boundaries.

To simulate wave motion during the storm surges, wave parameters obtained from the wave buoy DWRG1 (significant wave height, mean wave direction, peak period, wave spreading), weather data from the Paloma station (wind speed and direction, air temperature, precipitation), and water level obtained from the Trieste tide gauge at Molo Sartorio were used. Wind, air temperature, and water level were set as varying in time and constant in the domain, while wave parameters were set constant along the Adriatic boundary.

The mesh was interpolated starting from the bathymetry of the Gulf of Trieste, obtained from the bathymetric model of the European Marine Observation and Data Network (EMODnet) of 2022 [89] on a grid of 1/16 × 1/16 arc minute of longitude and latitude (ca. 115 × 115 m) integrated with the bathymetric model provided by [90] and higher resolution bathymetric models of the northern coastal area on a grid of 2 × 2 m.

4.2. Orthomosaics and DEMs Creation and Point Cloud Comparison

4.2.1. UAV Survey

The UAV used for the acquisition was a DJI Mavic 3T (DJI Enterprise series). The Mavic 3T is equipped with a 48 MP and 1/2″ CMOS camera sensor with an f/2.8 wide angle lens (24 mm equivalent), stabilized by a 3-axis gimbal. The drone was equipped with a DJI RTK (Real Time Kinematic) module (Mavic 3 Enterprise series), which provided NRTK-corrected (Net Real Time Kinematic) GNSS positioning data, enabling accurate georeferencing of each image. This module has a horizontal nominal accuracy of 1 cm (+1 ppm) and a vertical nominal accuracy of 1.5 cm (+1 ppm).

UAV surveys were carried out on 29 September, 27 October, 7 November, 29 November, 4 December 2023, and on 13 February 2024. All acquisitions were conducted with pre-planned and self-consistent surveys defined using the DJI Pilot 2 application (version 1.1.5). The flights were designed to maintain a constant flight route altitude of 90 m a.s.l. (considering the EGM96 geoid as the sea level), with the camera pointed orthogonally to the ground. Acquisitions were planned, maintaining a side and a frontal overlap ratio between images of 85% and a flight speed of 7 m/s. A total of 471 images were acquired for each survey.

4.2.2. GNSS Survey

To improve the georeferencing accuracy of models and to facilitate comparison between them, 11 Ground Control Points (GCPs) were chosen. Their locations were acquired using a Leica GS07 GNSS antenna in an NRTK configuration, utilizing real-time corrections provided by the GNSS net Hexagon (HxGN) SmartNet. The Leica GS07 GNSS antenna, supported by an RTK net, can reach a horizontal accuracy of 10 mm (+0.5 ppm) and a vertical accuracy of 20 mm (+0.5 ppm). The recording of GCPs was set to be carried out when the accuracy of planar and quote coordinates was less than 3 cm.

4.2.3. SfM-MVS Photogrammetry

The UAV image processing was conducted using Agisoft Metashape 2.0.1. This software is renowned for its reliability and widespread adoption in the field of 3D reconstructions from digital imagery [100]. The processing workflow of each set of images was performed independently in Metashape, where the alignment process was configured to high accuracy and no point limit settings. This initial stage entails the employment of SfM algorithms [101] to retrieve the spatial coordinates of points within the scene by correlating and subsequently analyzing the 2D pixel coordinates across various images [102,103]. The resulting matched tie points form a sparse point cloud that represents the reconstructed scene. The georeferencing was provided by both the RTK position of the images and by the GCPs. Subsequently, iterative steps of gradual selection filtering of points and camera optimization were conducted to enhance the quality of the model (e.g., [104]). Specifically, the point cloud was filtered using gradual selection tools of Metashape based on reconstruction uncertainty, projection accuracy, and reprojection error. After each filtering step, cameras were optimized, resulting in an overall significant decrease in the estimated error associated with the SfM reconstruction of the GCP positions. The subsequent phase involved the calculation of the image depth maps and the creation of multitemporal DEMs and orthomosaics of the study site. DEMs and orthomosaics obtained after the application of the described workflow to the different sets of images show a resolution of about 6.3 cm (≈250 points/m^2) and 2.9 cm, respectively.

Within a sub-area focused on the studied landforms, the multitemporal point clouds were densified using the point cloud building step of Metashape, which relies on Multi-View Stereo (MVS) algorithms [105], thereby completing the comprehensive SfM-MVS photogrammetry workflow [59,106]. Before cloud-to-cloud comparison, the sub-models were re-aligned by registering using only the GCPs positions, thus minimizing georeferencing error between different acquisitions. Finally, the cloud-to-cloud comparison between dense point clouds was carried out using CloudCompare (version 2.14.4), an open-source software for point cloud processing and analysis (available at [107]).

4.3. HR 3D Models Creation

4.3.1. UAV Survey

To acquire HR 3D models of the studied storm-induced landforms, a different UAV device was used: a DJI Mini 3 Pro equipped with a 3-axis gimbal-stabilized 48 MP and 1/1.3″ CMOS camera sensor with an f/1.7 lens (24 mm equivalent). The low weight and compact size of this UAV made it ideal for flights at lower altitudes and closer proximity to the target scene.

The flights were conducted on 29 November 2023, when the studied landforms (sinkholes C, F, G in SECTOR 1 and H in SECTOR 2) were at their maximum extent, except for the sinkhole H, for which the restoration works had already begun (Figure 2). The flights were carried out manually, ensuring that all images depicted the chosen subjects from various angles. Georeferencing of the images was provided by the standalone GNSS system equipped on the UAV (without RTK correction), ensuring an accuracy of a few meters (e.g., [108,109]). Correct scaling of these models was granted by adding four markers at known distances, employing the methodology established by Corradetti [110]. The relative distances between the markers were measured using a laser distance meter (model Bosch GLM 50–27 CG Professional), which has a nominal measuring accuracy of ± 1.5 mm, corresponding to the scale accuracy of the HR 3D models.

4.3.2. SfM-MVS Photogrammetry

The processing of these subsets of UAV images was performed using the Metashape software (version 2.0.1), replicating most of the workflow already described in Section 4.2.3. The main difference was the absence of accurate positioning of the images during the registration of models, which was provided by the known relative distances between the markers. In addition, these HR 3D models were also meshed and textured, achieving a final ground resolution between 2.33 and 3.34 mm/pix (value provided by Agisoft Metashapefinal reports).

5. Results

5.1. Wave Modelling

Between late October and early November 2023, the coastal area of the Gulf of Trieste was hit by 6 storm events with significant intensity and wave height (exceeding 2 m, according to DWRG1 recordings). These storms caused extensive damage along the entire coast, particularly in the area of Sistiana Mare, where eight sinkholes formed, severely damaging the existing man-made structures. Since no wave-monitoring systems are present near Sistiana Mare, wave motion in the Gulf of Trieste from 27 October to November 9 was simulated through the spectral wave module of MIKE 21 2024 Update 1 modeling software, and the time series of the significant wave height was extracted at the study area (13.63°E, 45.76°N, 10 m depth).

Of the six peaks representing the storm events, only the four originating from SW winds produced waves impacting the coastline with Hs greater than 1 m (Table 3). These storms occurred on 27 October (EVENT 1) and 31 (EVENT 3) and on 3 November (EVENT 5) and 5 (EVENT 6) (Figure 6). In the two events with waves and wind from the south, which occurred on 30 October (EVENT 2) and 2 November (EVENT 4), the Hs was dampened by about 70% compared to the DWRG1 buoy data due to the misalignment of wind and offshore waves relative to the longest fetches. EVENTs 1 and 3 experienced similar nearshore wave attenuation of about 40%, despite differing wave and wind characteristics. The first was characterized by offshore wave motion from SSE (170°N) and SW winds (220°N) up to 15.0 m/s, while the latter experienced waves coming from SSW (205°N) and wind blowing from WSW (265°N) up to 13.9 m/s. The most severe storm at Sistiana Mare was the fifth (3 November). During this storm, SSW wave motion (197°N) and SW winds (221°N) blowing up to 18.3 m/s were able to generate the highest nearshore waves, reaching up to 1.8 m of Hs, resulting in the least damped event with only a 33% nearshore attenuation. Finally, the last event (5 November), characterized by waves from SSE (172°N)

and wind up to 14.7 m/s from SW (235°N), was significantly dampened (71%), producing waves with Hs up to 1.08 m near the coast, although the waves recorded at DWRG1 were the highest, reaching up to 3.77 m.

Table 3. Storm events: marine characteristics simulated through MIKE21 Spectral Waves by ©DHI at Sistiana Mare. Hs is the significant wave height.

Storm Event	Storm Date	Hs at Sistiana Mare [m]	Hs Sistiana Mare/HS DWRG1 (%)	Time over 1 m Threshold [Hours:Minutes]
EVENT 1	27 October 2023 06:00	1.30	58%	3:50
EVENT 2	30 October 2023 20:30	0.67	29%	-
EVENT 3	31 October 2023 13:00	1.24	60%	2:00
EVENT 4	2 November 2023 17:30	0.97	30%	-
EVENT 5	3 November 2023 14:00	1.81	67%	8:35
EVENT 6	5 m November 2023 03:00	1.08	29%	1:05

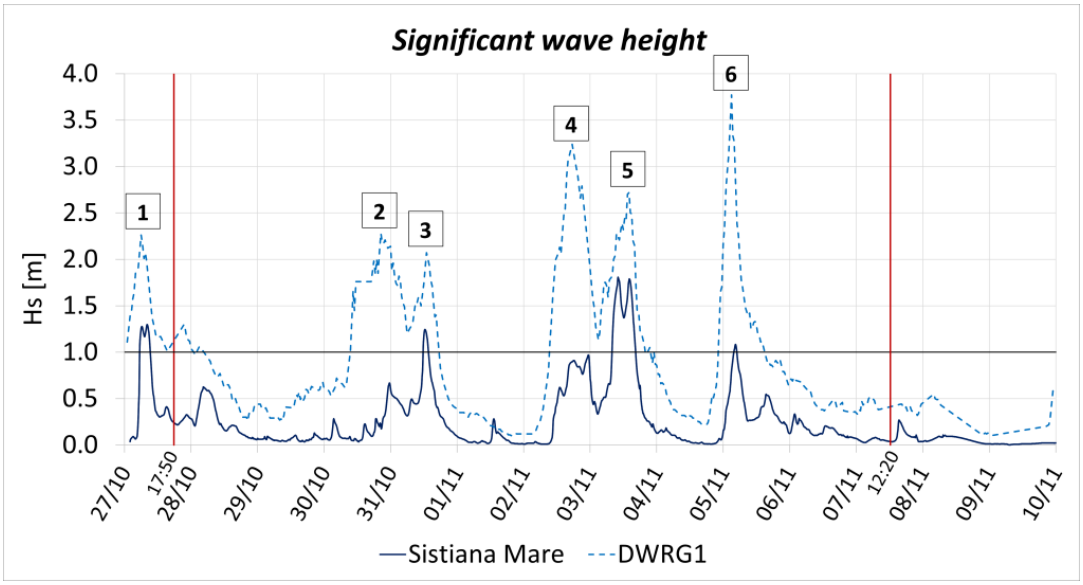

Figure 6. Graph representing the significant wave height recorded at the DWRG1 buoy (open sea, light blue dashed line) and simulated through MIKE21 Spectral Waves by ©DHI at the study area (Sistiana Mare, dark blue line). The different storm surge events are here indicated with their corresponding numbers (from 1 to 6 and refers to those of Tables 2 and 3). UAV surveys of 27 October, following the first event, and 9 November, following the whole multi-event, are evidenced (vertical red lines).

At Sistiana Mare, the significant wave height exceeded the threshold of 1 m for a total of 15 h and 30 min: 3:50 h during EVENT 1, prior to the second UAV survey (29 October), and 11 h and 40 min between surveys 2 and 3 (9 November), divided among EVENT 3 (2 h), EVENT 5 (8 h and 35 min), and EVENT 6 (1 h and 5 min).

5.2. Observations on Orthomosaics and DEMs

Using UAV surveys and the associated products obtained (orthomosaics, DEMs, and 3D models), it was possible to monitor the formation and evolution of the eight sinkholes that occurred along the coast of Sistiana Mare, which were identified (Figures 7–9) and measured (Table 4). For clarity, the formed sinkholes were named in alphabetical order from west to east.

Table 4. Geometric characteristics of the identified sinkholes at their maximum extension were measured on 4 December, except for sinkhole H, whose maximum dimensions were measured on 7 November. The depth of sinkhole E (*) (as for the initial phase of sinkhole C) is underestimated due to the absence of light inside it, which did not allow an efficient application of SfM methods.

Sinkhole	Major Axis (a) [m]	Minor Axis (b) [m]	Flattening Factor ($1-\frac{b}{a}$)	Maximum Depth [m]	Perimeter [m]	Area [m^2]
A	1.68	1.21	0.28	0.30	4.77	1.37
B	5.69	2.01	0.65	1.18	13.21	9.18
C	5.72	3.64	0.36	1.87	15.81	17.04
D	6.86	2.39	0.65	1.06	16.31	11.67
E	1.40	1.15	0.18	0.26 *	4.31	1.03
F	3.24	2.12	0.35	0.84	8.75	5.39
G	3.89	3.68	0.05	0.80	13.28	9.88
H	5.84	2.87	0.51	1.68	14.79	13.05

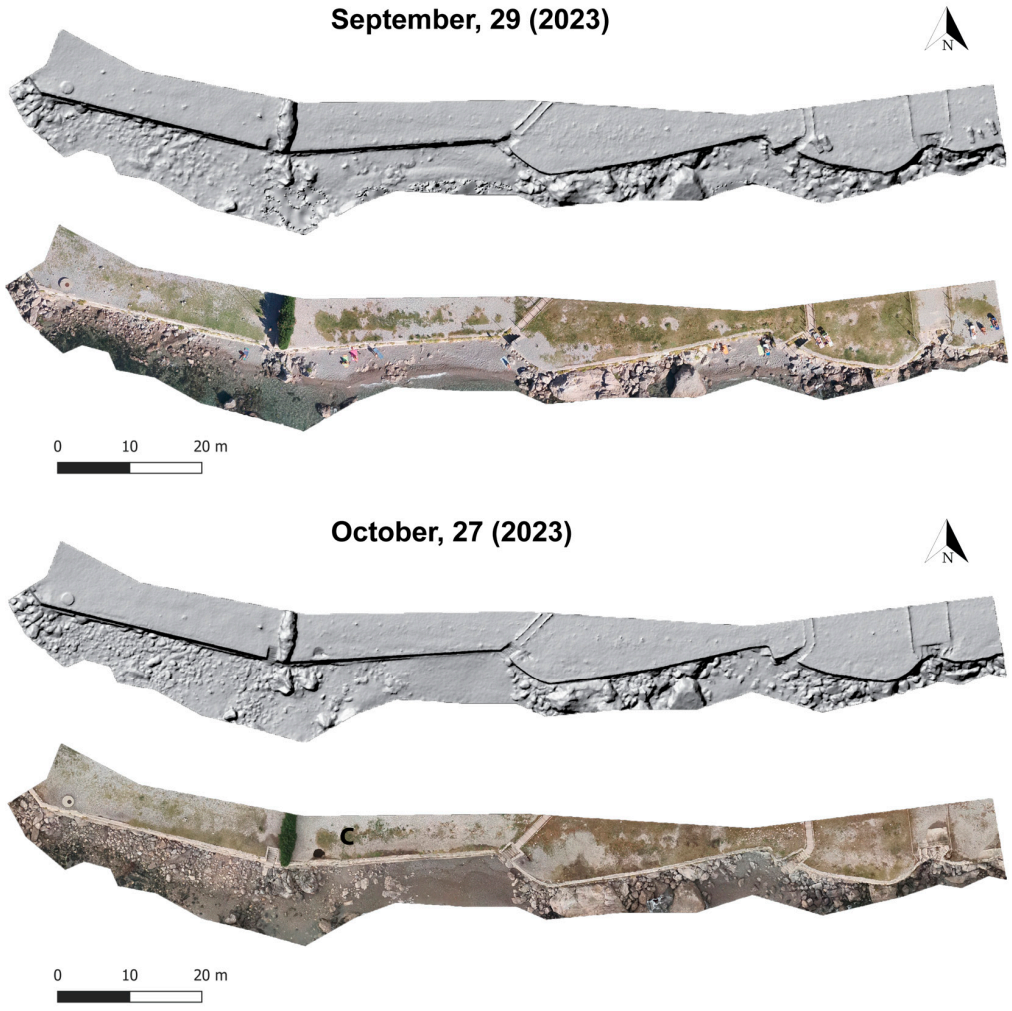

Figure 7. Caravella Beach shaded relief and orthomosaics (SECTOR 1) comparison between two different surveys: pre-storm event of 29 September (2023) and on 27 October (2023), just after the EVENT 1. The storm surge event that occurred during the night between 26 and 27 October (2023) produced the opening of only one sinkhole, the one identified with letter C, but also caused the removal of the finest material along the beach and in particular in its western part.

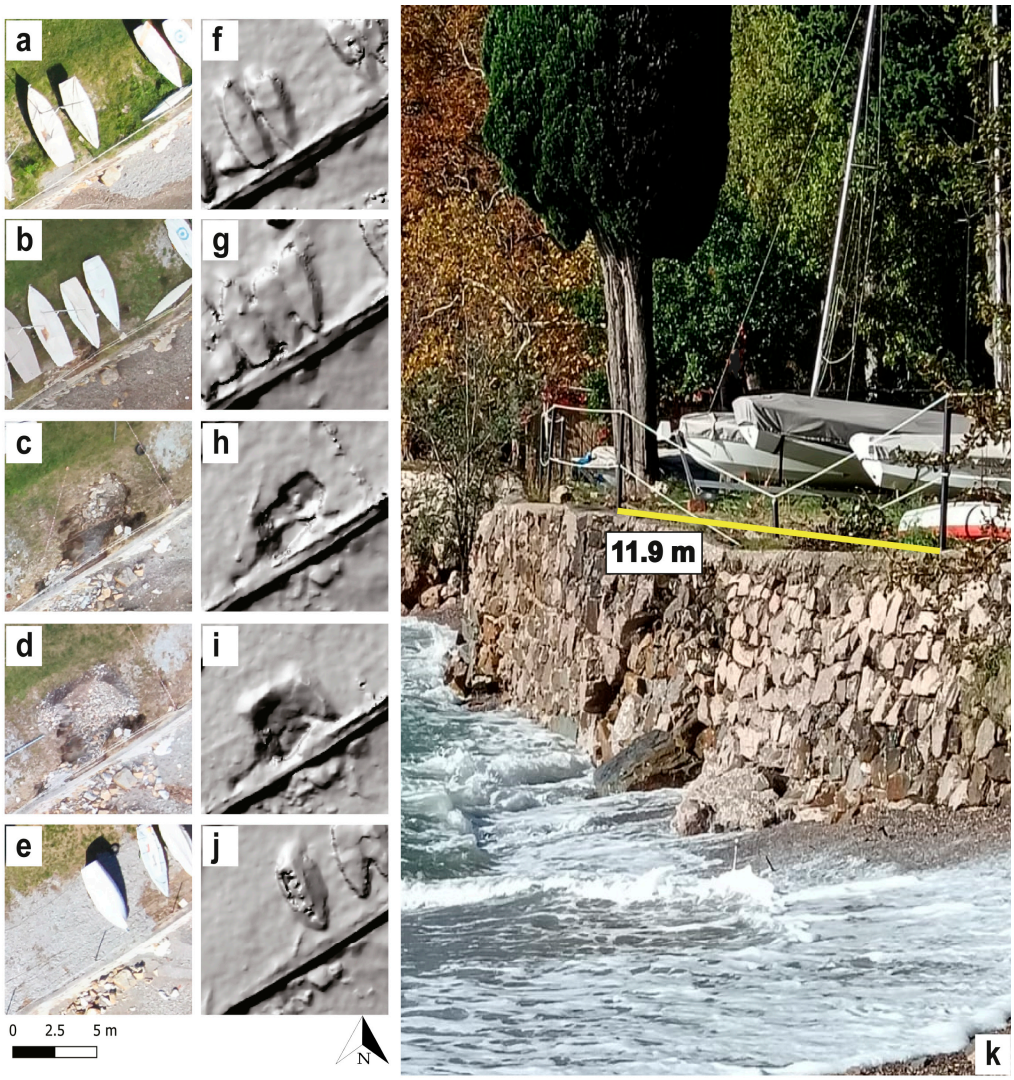

Figure 8. Orthomosaics (**a**–**e**) and shaded relief (**f**–**j**) representing sinkhole H. The scene depicted represents sinkhole H on 29 September 2023 (**a**,**f**), on 27 October 2023 (**b**,**g**), on 7 November 2023 (**c**,**h**), on 4 December 2023 (**d**,**i**) and on 27 February 2024 (**e**,**j**). (**k**) A detail of the collapsed retaining wall on 28 October.

The UAV survey realized on 27 October, and the derived orthomosaics and shaded relief allowed the evaluation of the effects of storm EVENT 1, which caused the opening of the first sinkhole (identified as sinkhole C) (Figure 7). The estimated void had an area of 1.61 m^2 (more than ten times smaller than its maximum extent reached on 4 December, equal to 17.04 m^2) and a flattening factor (defined as the difference in magnitude between the semimajor and the semiminor axis divided by the semimajor axis) of 0.26 (Table 4) (lower than that measured at its final stage, equal to 0.36). Data comparison between the two UAV acquisitions (29 September and 27 October) captured the formation stage of this sinkhole, revealing a circular surface shape. According to the DEM (Figure 7), the depth of sinkhole C was evaluated to be 0.5 m, though this is an underestimate due to the total absence of light inside it, which impaired the effectiveness of the Structure from Motion method and, consequently, the accurate depth reconstruction.

Sinkhole H was the only one that occurred in SECTOR 2 (Figure 2c). Orthomosaics and shaded relief representing this sector after EVENT 1 showed the formation of a depression beneath the boats (Figure 8b,g). Unfortunately, the presence of boats parked in the embanked area obscured the depressed feature, making it difficult to clearly evaluate the slopes of its side walls. A photograph taken the day after EVENT 1 (Figure 8k) shows

the collapse of the retaining wall and the creation of the sinkhole (the iron pole inside the sinking feature is not aligned with the other two placed outside).

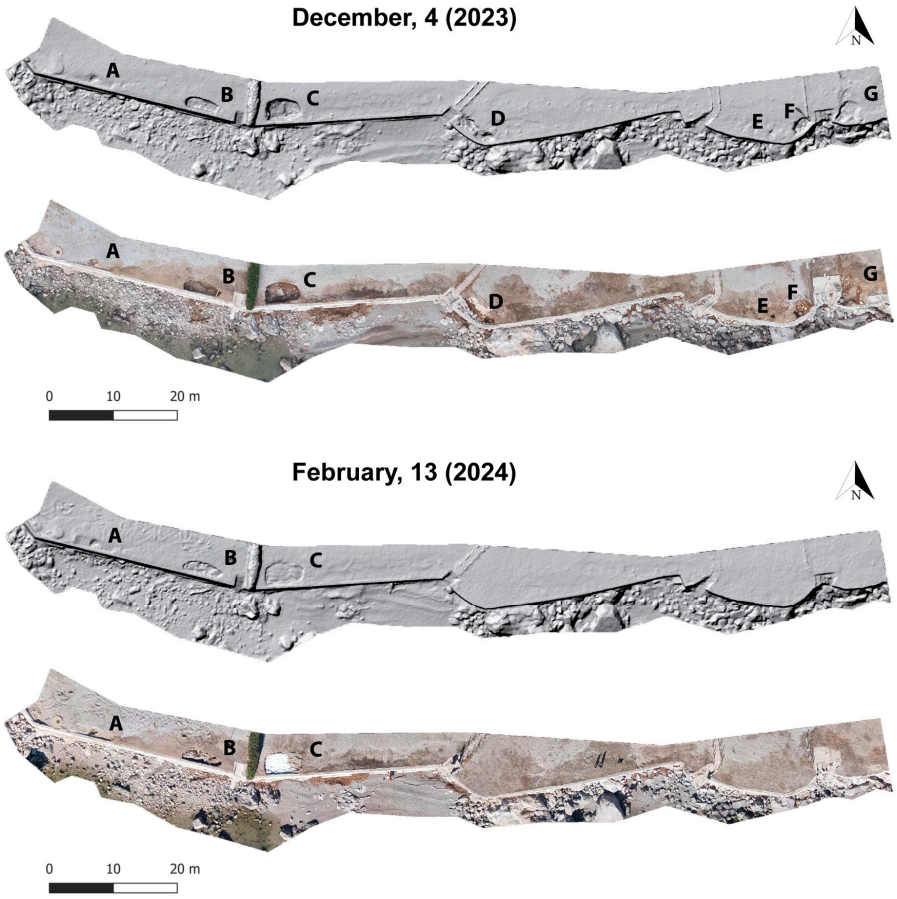

Figure 9. Caravella Beach shaded relief and orthomosaics (SECTOR 1) comparison between two different surveys: 4 December (2023) and 13 February (2024). The storm surge events between 31 October and 5 November (2023) caused the occurrence of most of the sinkholes in this sector (A, B, D, E, F, and G) and enlarged sinkhole C. The last acquisitions on 13 February show the ongoing restauration phase, with the leveling of the embankment behind the retaining wall and the consequent disappearance of sinkholes D, E, F, and G and the beach replenishment (mainly in front of sinkhole C).

The subsequent series of five storm surge events caused the paroxysm of all the other sinkholes in both sectors (Figure 8c,h, and Figure 9).

Unfortunately, due to adverse weather conditions, further UAV surveys were not possible until 7 November. Since the orthomosaics and shaded relief associated with acquisitions performed on 7 November and 4 December showed only negligible differences in the features, the acquisitions of 4 December were considered to represent the final evolutionary stage of sinkholes before the start of restoration activities (Figure 8e–j). Overall, the DEMs reveal that different sinkholes exhibit distinct geometries and varying degrees of erosion. For instance, Sinkhole A (Figure 9) displays an early stage of development with gently sloping sides.

By 13 February, restoration works were underway across the entire study area. Sinkholes D, E, F, and G (Figure 9) had already been filled, and the embankment had been levelled. Additionally, the replenishment of gravel beaches had begun, particularly on the stretch in front of sinkhole C.

Thanks to the use of UAVs, orthomosaics, DEMs, and point clouds, the most important morphometric parameters for each phenomenon were obtained and later validated by on-site manual measurements. The geometrical characteristics at the phase of maximum

detected expansion are summarized in Table 4. They have variable dimensions and show that, while the smaller ones maintain a circular shape (low flattening factor), the larger ones tend towards an elliptical shape (with a higher flattening factor), aligning parallel to the retaining wall.

5.3. HR 3D Models

To better understand the dynamic of sinkhole occurrence, three HR 3D models were reconstructed and analyzed (Figures 10 and 11). The 3D model of sinkhole B, reconstructed after all the storm events on 29 November (Figure 10a), revealed that the stone retaining wall upstream of the beach, including its curb foundations, appeared to be intact (label 1 in Figure 10a). However, beneath it, a horizontally elongated excavation was observed (label 2 in Figure 10a). The analyzed sinkhole was characterized by an area of 9.18 m^2, a maximum depth of 1.18 m, and a flattening factor of 0.65.

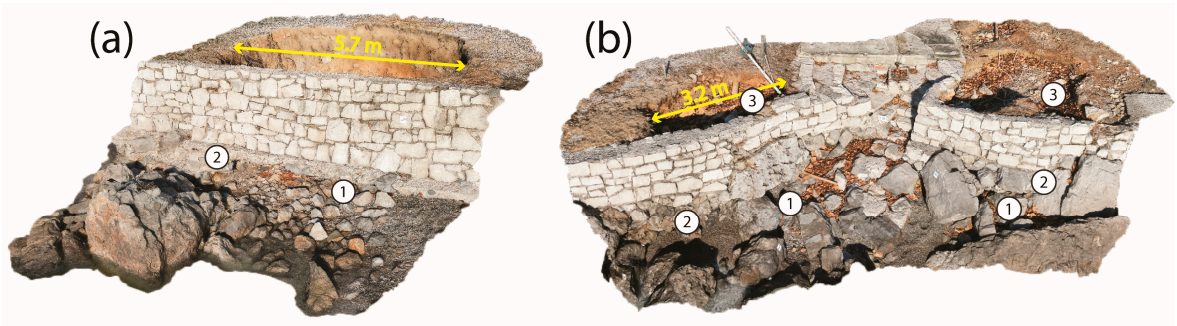

Figure 10. (**a**) HR 3D model of sinkhole B on 29 November 2023 (https://skfb.ly/p7U7E, accessed on 21 August 2024); (**b**) HR 3D model of sinkholes F and G on 29 November 2023 (https://skfb.ly/p7Uws, accessed on 21 August, 2024). (1) foundations of the retaining wall; (2) horizontally elongated hole; (3) collapsed material. View towards North. The ground resolutions of the models (provided by Agisoft Metashape reports) are respectively 2.86 (**a**) and 2.33 mm/pix (**b**).

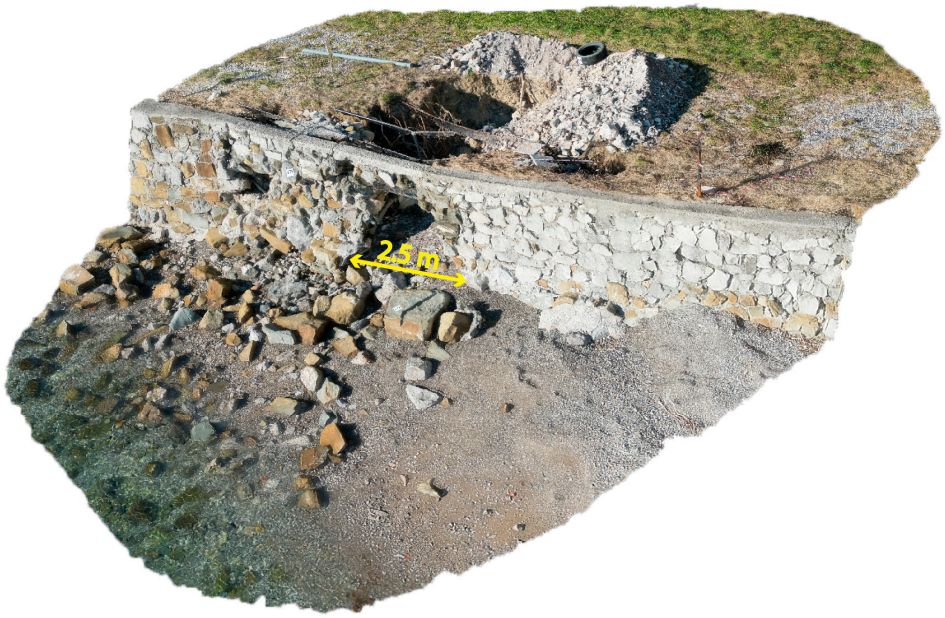

Figure 11. Three-dimension model of the sinkhole H on 29 November 2023 (https://skfb.ly/p7Uzu, accessed on 21 August 2024). It was already partially filled with landfill material. The retaining wall is almost completely broken. View towards the north-west. The ground resolution of the model (provided by the Agisoft Metashape report) is equal to 3.34 mm/pix.

Considering the 3D model of sinkholes F and G (Figure 10b), their area is equal to 5.39 and 9.88 m^2, with maximum depths of 0.84 and 0.80 m and flattening factors of 0.35 and 0.05, respectively. The model analysis reveals similar characteristics to those previously described for sinkhole B. In both cases, the sinkholes are confined by the intact retaining wall, and a linear hole is present beneath them. In this sector, the wall is built directly on large boulders, with its foundations merged into them.

Sinkhole H presents a depressed landform that had already partially filled with landfill material (Figure 11), as restoration works for sinkhole H had already begun on 29 November (Figure 8e,j). In this case, the retaining wall is almost completely broken, its foundations remain covered, and no under-excavation voids are present.

This landform is one of the largest in the entire study area and is characterized by an area of 13.05 m^2, a maximum depth of 1.68 m, and a flattening factor of 0.51.

5.4. Point Clouds Comparison

The cloud-to-cloud comparison between dense point clouds contributed to shed further light on the evolution of SECTOR 1, but offered limited information for SECTOR 2, where some boats covered sinkhole H during the acquisition days.

By analyzing the difference between the point clouds of 29 September and 27 October 2023 (Figure 12a), the effects of storm EVENT 1 become evident. In addition to the formation of sinkhole C, which was previously identified through the analysis of orthomosaics and shaded relief, the applied method highlights the concentration of surge erosion in the areas in front of the retaining wall, where sinkholes B, C, and D subsequently appeared (identified with number 1 on Figure 12a,b). On the embankment, in the areas identified with number 3, small depressions elongated in the direction of the retaining wall are already present, acting as precursor signs of further collapses. Despite the predominance of erosional processes on the beach during the first storm event, a zone of gravel sediment accumulation just in front of the wall is present in the middle of SECTOR 1 (identifiable with number 2 in Figure 12a).

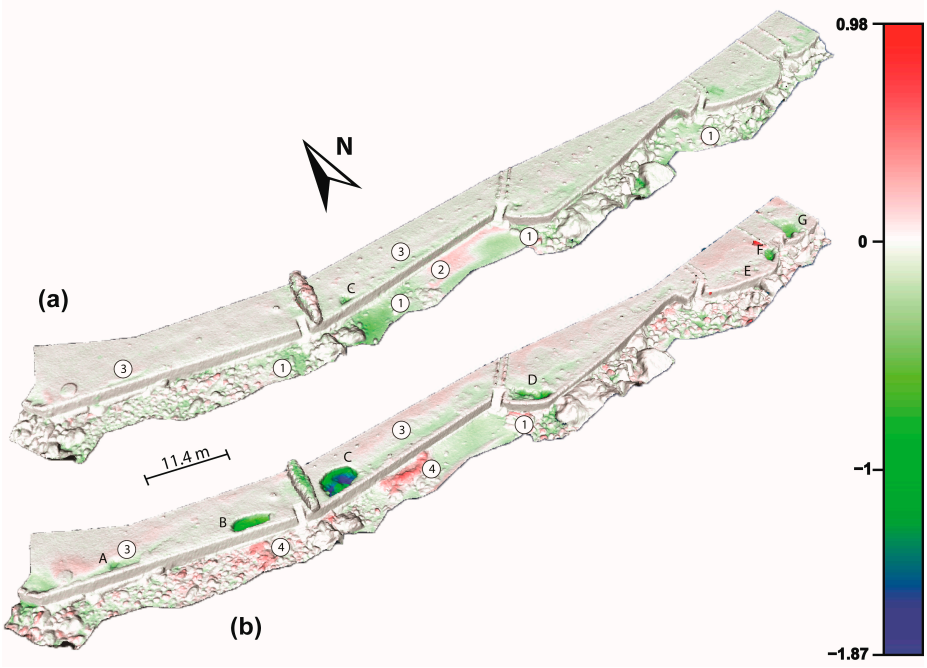

Figure 12. Cloud-to-cloud comparison between dense point clouds of (**a**) 29 September (2023) and 27 October (2023) and (**b**) between 27 October (2023) and 4 December (2023). Highlighted in green are the areas where the wave erosion was concentrated (1); in red are the areas of accumulation of gravel sediments (2) after EVENT 1, and the wooden material accumulation (4) occurred after the last four storm events hit Caravella Beach. Number (3) identifies the linear depressions located immediately beyond the retaining wall and parallel to it.

In the area in front of sinkhole D, erosion is present in both point cloud comparisons, denoting a higher continuity of the process during all surge events impacting the beach. Furthermore, the accumulation of wooden material in front of the retaining wall is also evident (Figures 9 and 12b, number 4). Finally, in both the models' comparisons, a slight deformation immediately beyond the wall and parallel to it is visible (Figure 12 number 3), highlighting the pervasiveness of storm surge erosion along the entire western part of the area considered.

6. Discussion

The formation of coastal sinkholes in Sistiana Mare during the storm events of late 2023 underscores the vulnerability of coastal areas in the northern Adriatic to extreme meteorological conditions. The results obtained through UAV monitoring and wave modeling provide critical insights into both the processes driving sinkhole formation and the potential mitigation strategies.

6.1. Wave Modelling

The model of the series of storm events highlights that the nearshore significant wave height is not always proportional to open sea data recorded by the DWRG1 wave buoy. Indeed, the modeling revealed that nearshore the Hs at Sistiana Mare is strongly influenced by both the offshore wave motion and wind characteristics in terms of intensity and direction (Figure 6). Specifically, events generated by winds and involving waves with directions not aligned with the longest fetches (from 220°N to 190°N) (Figure 3) were significantly dampened compared to their intensity at the DWRG1 buoy. This was the case for the second (31 October), fourth (2 November), and sixth (5 November) events (Figure 6). On the other hand, when both offshore waves and wind are directed within the major fetches, as occurred during EVENT 5, the nearshore waves can be quite high, capable of delivering substantial energy to the shoreline and the existing infrastructure. However, such events are uncommon in the northern Adriatic, as shown by the recordings from the DWRG1 wave buoy (Figure 4), making them exceptional occurrences for the Gulf of Trieste.

6.2. Coastal Sinkhole Formation

The study revealed the progressive development of coastal sinkholes in Sistiana Mare during six main storm events that hit the area. The analysis of orthomosics and shaded reliefs reveals that the storm event on 27 October (EVENT 1) created the conditions for the subsequent openings of the remaining sinkholes in SECTOR 1 by removing fine material from Caravella Beach, leaving only larger particles such as pebbles and boulders (Figure 7). In the areas where the most aggressive erosion occurred, small evidence of surface accommodations was already visible during the survey on 27 October. Subsequently, sinkholes developed in some of these locations (Figure 9).

The coastal erosion caused by the subsequent storm surges removed finer material, eventually leading to under-excavation of the stone retaining walls and the formation of sinkholes. This process was particularly evident in the formation and enlargement of sinkhole C, which evolved from a small circular depression into one of the largest features.

The DEM analysis of sinkhole A after all events, evidencing gentleness of the sinkhole sides suggests a plastic behavior, leading to a gradual accommodation of the ground surface as it deformed smoothly over the underlying void. This feature could still represent an initial evolutionary stage, indicating that the collapse forming sinkholes occurs only when a critical threshold of underlying material loss is reached. The elliptical shape linked to the final evolutionary stage is due to the linear shape of the wall, which acts as a constraint.

In SECTOR 2, sinkhole H showed subsiding evidence after EVENT 1 (Figure 8). Despite the presence of boats to hinder the true characteristics of the sinkhole, a certain gentleness in the slopes could indicate that this landform corresponded to an initial stage of the future sinkhole. Similarly, the analysis of the HR 3D model of sinkhole B (Figure 10a), characterized by an intact retaining wall and a horizontally elongated excavation under-

neath, indicates that the genesis of the sinkhole was linked to diffuse wave erosion, which initially removed the finer material and subsequently caused the under-excavation of the man-made structure. The verticality of the sinkhole's walls suggests an initial sagging followed by a collapse mechanism. The absence of the collapsed material is due to its subsequent removal by waves and marine tides. The presence of large boulders in front of the beach, though detached from the retaining wall, partially protected the man-made structure by dampening significantly Hs.

The characteristics of sinkholes F and G (Figure 10b), along with the verticality of their walls, suggest a similar genesis to that of sinkhole B. The only appreciable difference is that sinkholes F and G contain a considerable amount of collapsed material. The presence of this material can be explained by a lower vulnerability of the site to wave impacts, higher protection from erosive action due to the greater presence of boulders, and/or a later occurrence of the collapse, which allowed the waves to remove only a small portion of the material.

A slightly different scenario is observed when analyzing the HR 3D model of sinkhole H (Figure 11), where the retaining wall was almost completely broken and no under-excavation voids are present. After the removal of the finer components of the beach, the waves eroded the base of the wall, leading to its collapse. The absence of the concrete curb at the bottom of the retaining wall further facilitated its collapse.

The analysis of the difference between dense point clouds of 27 October (Figure 12a) and 4 December 2023 (after the entire series of subsequent storm events) (Figure 12b) in SECTOR 1 confirms the predisposing effect of the first event on the sinkholes' formation. Indeed, in the area where sinkholes B and C formed, the model shows a decrease in beach erosion, the occurrence of sinkhole B, and the expansion of sinkhole C. The wave energy was no longer used to remove the fine material from the beach but to under-excavate the retaining wall, causing the appearance of horizontal voids and, consequently, collapses.

6.3. Protective Role of Boulders

This study also evidenced the protective role of boulders in mitigating the impact of storm surges. Indeed, data analysis of SECTOR 1 (Figure 9) revealed that sinkholes were more concentrated in areas lacking large carbonate boulders in front of the stone retaining wall. These boulders acted as a natural barrier, preserving the man-made retaining wall by preventing the under-excavation of the structure and the consequent collapse of the loose material. Thus, the appearance of sinkholes was influenced not only by the characteristics of the events (with wave direction ranging from SSE to SSW) but also by geomorphological factors, such as the presence of stone-retaining walls partially protected by boulders embedded in the beaches.

7. Conclusions

The phenomenon of coastal sinkholes, though little studied, has proven to be particularly relevant in the coastal sector of the northern Adriatic Sea. This area, notably including the Venice lagoon, has been extensively studied concerning issues related to sea level rise. However, limited information exists regarding the impacts of storm events in surrounding areas, such as the Trieste waterfront analyzed in this study. The storm events of autumn 2023 provided an opportunity to shed light on the vulnerability of these coasts, enabling researchers to monitor the occurrence and evolution of specific features using Unmanned Aerial Vehicles (UAVs).

Damages to the coastline and the man-made structures in these locations are generally rare: only events characterized by winds from 190°N to 220°N, uncommon meteorological conditions in the northern Adriatic Sea, have the longest fetch to generate high and energetic wave motion with the right impact angle relative to the coastline orientation. The multi-event that occurred in autumn 2023 represents a rare example of a SW-storm, during which the significant wave height exceeded the 1-m threshold nearshore for 15 h and 30 min, reaching up to 1.81 m.

The six UAV flights conducted between 29 September 2023 (with the availability of a crucial baseline acquisition before the storm events) and 14 February 2024 enabled the creation of orthomosaics, shaded reliefs, 3D models, and point cloud comparisons. These tools were instrumental in clarifying the genesis of the eight coastal sinkholes that formed in Sistiana Mare. The area, characterized by gravel beaches with a limited backshore (<10 m) and landward retaining stone walls, experienced six storm events that resulted in:

- Preliminary removal of finer material from the beaches;
- Under-excavation of the retaining stone walls, causing sagging of the landward embankment behind the retaining wall;
- Subsequent collapse of the materials, including the destruction of the retaining wall in the most representative case of sinkhole H.

The study highlighted several advantages of using UAV remote sensing technology for coastal monitoring, including:

- Fast and precise damage assessment, as UAVs allow for rapid HR morphometric analysis and assessment of damage, which can be crucial for timely and effective response and restoration efforts;
- Monitoring over time, as repeated UAV surveys allow for the tracking of tem-poral changes, facilitating long-term observation of coastal dynamics as well as the assessment of catastrophic events.

One significant outcome of this study was the assessment of the protective role exerted by boulders placed at sea in front of the retaining walls. These boulders can serve as a fundamental defense for the coasts; their presence mitigated the severity of coastal sinkhole formation and protected the integrity of the retaining walls.

This study was made possible in part due to the availability of a baseline, underscoring the critical importance of conducting regular monitoring studies along coastal areas that may be susceptible to such events. With climate change, these events are likely to become more frequent and severe, making it even more crucial to understand their evolution. Periodic monitoring allows for a detailed and in-depth understanding of these phenomena and provides essential data to enhance coastal protection strategies. By establishing a continuous and systematic observation framework, we can implement more effective measures to mitigate the impacts of future events, thereby safeguarding coastal environments and communities that depend on them.

Author Contributions: Conceptualization, C.C., A.B. and C.L.; methodology, C.L., S.F., P.R. and S.S.; software, C.L., S.F. and S.S.; validation, A.C.; data curation: A.C. and C.L.; investigation, C.L., A.B. and P.R.; data curation, C.L.; writing—original draft preparation, C.C., C.L., A.B., P.R., S.F., S.S. and A.C.; writing—review and editing, C.C., C.L., A.B., P.R., S.F., S.S., A.C. and L.Z.; funding acquisition, L.Z. and C.C. All authors have read and agreed to the published version of the manuscript.

Funding: This research was funded by Servizio Geologico Friuli Venezia Giulia Region in the framework of the following projects: (1) Grant number CUP J95F21002770002 "Realizzazione dei Fogli geomorfologici alla scala 1:50.000 n. 110 Trieste e n. 131 Caresana della Carta Geologica ufficiale d'Italia e per lo studio geomorfologico applicato del territorio regionale e relativa cartografia", scientific coordinator Prof. Luca Zini; (2) grant number ALP-B/10/AG—447 "Aggiornamento continuo del censimento e della pericolosità dei sinkhole del territorio regionale", scientific coordinator Prof. Chiara Calligaris. Part of this study was funded by the consortium iNEST (Interconnected North-Est Innovation Ecosystem) funded by the European Union Next-GenerationEU (Piano Nazionale di Ripresa e Resilienza (PNRR)-Missione 4 Componente 2, Investimento 473 1.5-D.D. 1058 23/06/2022, ECS_00000043).

Data Availability Statement: All the data/models used in this study can be made available upon request to interested parties.

Acknowledgments: The authors would like to thank the scientific coordinators of the abovementioned projects, functionaries of the Geological Survey of the Friuli Venezia Giulia Region, in the persons of Chiara Piano.

Conflicts of Interest: The authors declare no conflicts of interest. The funders had no role in the design of the study, in the collection, analysis, or interpretation of data, in the writing of the manuscript, or in the decision to publish the results.

References

1. MedECC. Climate and Environmental Change in the Mediterranean Basin–Current Situation and Risks for the Future. In *First Mediterranean Assessment Report 2020*; Cramer, W., Guiot, J., Marini, K., Eds.; Union for the Mediterranean, Plan Bleu, UNEP/MAP: Marseille, France, 2020; p. 632. ISBN 978-2-9577416-0-1.
2. Cramer, W.; Guiot, J.; Fader, M.; Garrabou, J.; Gattuso, J.P.; Iglesias, A.; Lange, M.A.; Lionello, P.; Llasat, M.C.; Paz, S.; et al. Climate change and interconnected risks to sustainable development in the Mediterranean. *Nat. Clim. Change* **2018**, *8*, 972–980. [CrossRef]
3. Lionello, P.; Scarascia, L. The relation of climate extremes with global warming in the Mediterranean region and its north versus south contrast. *Reg. Environ. Change* **2020**, *20*, 31. [CrossRef]
4. IPCC. Climate Change 2022: Impacts, Adaptation, and Vulnerability. In *Contribution of Working Group II to the Sixth Assessment Report of the Intergovernmental Panel on Climate Change*; Pörtner, H.-O., Roberts, D.C., Tignor, M., Poloczanska, E.S., Mintenbeck, K., Alegría, A., Craig, M., Langsdorf, S., Löschke, S., Möller, V., et al., Eds.; Cambridge University Press: Cambridge, UK; New York, NY, USA, 2022; p. 3056. [CrossRef]
5. Tuel, A.; Eltahir, E.A.B. Why is the mediterranean a climate change hotspot? *J. Clim.* **2020**, *33*, 5829–5843. [CrossRef]
6. Giorgi, F. Climate changes hot-spots. *Geophys. Res. Lett.* **2006**, *33*, L08707. [CrossRef]
7. Giorgi, F.; Lionello, P. Climate change projections for the Mediterranean region. *Glob. Planet Change* **2008**, *63*, 90–104. [CrossRef]
8. Xie, W.; Tang, B.; Meng, Q. The Impact of Sea-Level Rise on Urban Properties in Tampa Due to Climate Change. *Water* **2022**, *14*, 13. [CrossRef]
9. IPCC. *Climate Change 2021: The Physical Science Basis. Contribution of Working Group I to the Sixth Assessment Report of the Intergovernmental Panel on Climate Change*; Masson-Delmotte, V., Zhai, A.P., Pirani, S.L., Connors, C., Péan, S., Berger, N., Caud, Y., Chen, L., Goldfarb, M.I., Gomis, M., et al., Eds.; Cambridge University Press: Cambridge, UK; New York, NY, USA, 2021; p. 2391. [CrossRef]
10. Neumann, B.; Vafeidis, A.T.; Zimmermann, J.; Nicholls, R. Future coastal population growth and exposure to sea-level rise and coastal flooding—A global assessment. *PLoS ONE* **2015**, *10*, e0118571. [CrossRef]
11. Ranasinghe, R. Assessing climate change impacts on open sandy coasts: A review. *Earth Sci. Rev.* **2016**, *160*, 320–332. [CrossRef]
12. Nicholls, R.J.; Adger, N.; Hutton, C.W.; Hanson, S.E. *Deltas in the Anthropocene*; Palgrave Macmillan: Cham, Switzerland, 2020; p. 282. [CrossRef]
13. Vousdoukas, M.I.; Mentaschi, L.; Voukouvalas, E.; Verlaan, M.; Jevrejeva, S.; Jackson, L.P.; Feyen, L. Global probabilistic projections of extreme sea levels show intensification of coastal flood hazard. *Nat. Commun.* **2018**, *9*, 2360. [CrossRef] [PubMed]
14. Bakkensen, L.A. Mediterranean hurricanes and associated damage estimates. *J. Extreme Events* **2017**, *4*, 1750008. [CrossRef]
15. Portmann, R.; González-Alemán, J.J.; Sprenger, M.; Wernli, H. How an uncertain short-wave perturbation on the North Atlantic wave guide affects the forecast of an intense Mediterranean cyclone (Medicane Zorbas). *Weather Clim. Dynam.* **2020**, *1*, 597–615. [CrossRef]
16. Scicchitano, G.; Scardino, G.; Monaco, C.; Piscitelli, A.; Milella, M.; De Giosa, F.; Mastronuzzi, G. Comparing impact effects of common storms and Medicanes along the coast of southeastern Sicily. *Mar. Geol.* **2021**, *439*, 106556. [CrossRef]
17. Sanuy, M.; Duo, E.; Jäger, W.S.; Ciavola, P.; Jiménez, J.A. Linking source with consequences of coastal storm impacts for climate change and risk reduction scenarios for Mediterranean sandy beaches. *NHESS* **2018**, *18*, 1825–1847. [CrossRef]
18. Lira-Loarca, A.; Cobos, M.; Losada, M.Á.; Baquerizo, A. Storm characterization and simulation for damage evolution models of maritime structures. *Coast Eng.* **2020**, *156*, 103620. [CrossRef]
19. Amores, A.; Marcos, M.; Carrió, D.S.; Gómez-Pujol, L. Coastal impacts of Storm Gloria (January 2020) over the northwestern Mediterranean. *NHESS* **2020**, *20*, 1955–1968. [CrossRef]
20. Cavaleri, L.; Bajo, M.; Barbariol, F.; Bastianini, M.; Benetazzo, A.; Bertotti, L.; Chiggiato, J.; Davolio, S.; Ferrarin, C.; Magnusson, L.; et al. The October 29, 2018 storm in Northern Italy–an exceptional event and its modelling. *Prog. Oceanogr.* **2019**, *178*, 102178. [CrossRef]
21. Jiménez, J.; Sanuy, M.; Ballesteros, C.; Valdemoro, H. The Tordera Delta, a hotspot to storm impacts in the coast northwards of Barcelona (NW Mediterranean). *Coast Eng.* **2018**, *134*, 148–158. [CrossRef]
22. Amarouche, K.; Akpınar, A.; Cakmak, R.E.; Houma, F.; Bachari, N.E.I. Assessment of storm events along the Algiers coast and their potential impacts. *Ocean Eng.* **2020**, *210*, 107432. [CrossRef]
23. Anfuso, G.; Postacchini, M.; Di Luccio, D.; Benassai, G. Coastal sensitivity/vulnerability characterization and adaptation strategies: A review. *J. Mar. Sci. Eng.* **2021**, *9*, 72. [CrossRef]
24. Melet, A.; Meyssignac, B.; Almar, R.; Le Cozannet, G. Under-estimated wave contribution to coastal sea-level rise. *Nat. Clim. Change* **2018**, *8*, 234–239. [CrossRef]
25. McEvoy, S.; Hassnoot, M.; Biesbroek, R. How are European countries planning for sea level rise? *Ocean Coast Manag.* **2021**, *203*, 105512. [CrossRef]

26. Harley, M.D.; Turner, I.L.; Kinsela, M.A.; Middleton, J.H.; Mumford, P.J.; Splinter, K.D.; Phillips, M.S.; Simmons, J.A.; Hanslow, D.J.; Short, A.D. Extreme coastal erosion enhanced by anomalous extratropical storm wave direction. *Sci. Rep.* **2017**, *7*, 6033. [CrossRef]
27. Biolchi, S.; Denamiel, C.; Devoto, S.; Korbar, T.; Macovaz, V.; Scicchitano, G.; Vilibić, I.; Furlani, S. Impact of the October 2018 Storm Vaia on Coastal Boulders in the Northern Adriatic Sea. *Water* **2019**, *11*, 2229. [CrossRef]
28. Parise, M. Sinkholes. In *Encyclopedia of Caves*, 3rd ed.; William, B., White, D.C., Culver, T.P., Eds.; Academic Press: Cambridge, MA, USA, 2019; pp. 934–942. [CrossRef]
29. Liso, I.S. Sinkhole occurrence and evolution, and seawater intrusion in a low-coastal setting of Apulia. *Ital. J. Eng. Geol. Environ.* **2024**, 197–204. [CrossRef]
30. Forth, R.A.; Butcher, D.; Senior, R. Hazard mapping of karst along the coast of the Algarve, Portugal. *Eng. Geol.* **1999**, *52*, 67–74. [CrossRef]
31. Bruno, E.; Calcaterra, D.; Parise, M. Development and morphometry of sinkholes in coastal plains of Apulia, southern Italy. Preliminary sinkhole susceptibility assessment. *Eng. Geol.* **2008**, *99*, 198–209.
32. Delle Rose, M.; Parise, M. Karst subsidence in south-central Apulia Italy. *Int. J. Speleol.* **2002**, *31*, 181–199. [CrossRef]
33. Delle Rose, M.; Parise, M. Slope instability along the Adriatic coast of Salento, southern Italy. In Proceedings of the IX International Symposium on Landslides, Rio de Janeiro, Brasil, 28 June 2004–2 July 2004; Volume 1, pp. 399–404.
34. Delle Rose, M.; Parise, M. Speleogenesi e geomorfologia del sistema carsico delle Grotte della Poesia nell'ambito dell'evoluzione quaternaria della costa Adriatica Salentina. *Atti E Mem. Comm. Grotte "E. Boegan"* **2005**, *40*, 153–173.
35. Delle Rose, M.; Federico, A.; Parise, M. Sinkhole genesis and evolution in Apulia, and their interrelations with the anthropogenic environment. *NHESS* **2004**, *4*, 747–755. [CrossRef]
36. Parise, M. I sinkholes in Puglia. In *I Fenomeni Naturali di Sinkhole Nelle Aree di Pianura Italiana*; Nisio, S., Ed.; Memorie descrittive della Carta Geologica d'Italia: Rome, Italy, 2008; Volume 85, pp. 309–334.
37. Del Prete, S.; Iovine, G.; Parise, M.; Santo, A. Origin and distribution of different types of sinkholes in the plain areas of Southern Italy. *Geodin. Acta* **2010**, *23*, 113–127. [CrossRef]
38. Margiotta, S.; Negri, S.; Parise, M.; Valloni, R. Mapping the susceptibility to sinkholes in coastal areas, based on stratigraphy, geomorphology and geophysics. *Nat. Hazards* **2012**, *62*, 657–676. [CrossRef]
39. Coratza, P.; Galve, J.P.; Soldati, M.; Tonelli, C. Recognition and assessment of sinkholes as geosites: Lessons from the Island of Gozo (Malta). *Quaest. Geogr.* **2012**, *31*, 25–35. [CrossRef]
40. Soldati, M.; Tonelli, C.; Galve, J.P. Geomorphological evolution of palaeosinkhole features in the Maltese archipelago (Mediterranean Sea). *GFDQ* **2013**, *36*, 189–198. [CrossRef]
41. The Scottish Sun. Available online: https://www.thescottishsun.co.uk/news/6634343/sinkhole-fife-coastal-path-west-wemyss-harbour/ (accessed on 23 April 2024).
42. Edinburghlive. Available online: https://www.edinburghlive.co.uk/news/edinburgh-news/east-lothian-locals-warned-huge-28012627 (accessed on 23 April 2024).
43. Chroniclelive. Available online: https://www.chroniclelive.co.uk/news/north-east-news/what-caused-giant-sinkhole-blyth-17049690 (accessed on 23 April 2024).
44. Independent. Available online: https://www.independent.co.uk/tv/climate/huge-sinkhole-appears-at-coastal-beauty-spot-revealing-hidden-underground-beach-b2195003.html (accessed on 23 April 2024).
45. Newsweek. Available online: https://www.newsweek.com/coastal-sinkhole-suck-people-ocean-appears-overnight-1599411 (accessed on 23 April 2024).
46. The news tribune. Available online: https://www.thenewstribune.com/news/nation-world/national/article271602352.html (accessed on 23 April 2024).
47. OPB. Available online: https://www.opb.org/article/2023/05/20/2-sinkholes-have-appeared-on-oregons-north-coast-heres-more-on-why-they-happen/ (accessed on 23 April 2024).
48. MeteoWeb. Available online: https://www.meteoweb.eu/2021/12/maltempo-mareggiata-a-marsala-cede-tratto-del-lungomare/1746896/ (accessed on 23 April 2024).
49. In Alto Mare–Sant'Agata di Militello. Available online: https://www.facebook.com/inaltomare.santagata/ (accessed on 23 April 2024).
50. IlFattoVesuviano. Available online: https://www.ilfattovesuviano.it/2023/11/forti-mareggiate-crolla-la-litoranea-di-torre/#google_vignette (accessed on 23 April 2024).
51. Cooper, A.H. The classification, recording, databasing and use of information about building damage caused by subsidence and landslides. *QJEGH* **2008**, *41*, 409–424. [CrossRef]
52. Gutierrez, F. Sinkhole hazards. In *Oxford Research Encyclopedia of Natural Hazard Science 2016*; Oxford University Press: Oxford, UK, 2016. [CrossRef]
53. Calligaris, C.; Devoto, S.; Zini, L. Evaporite sinkholes of the Friuli Venezia Giulia region (NE Italy). *J. Maps* **2017**, *13*, 406–414. [CrossRef]
54. Busetti, A.; Calligaris, C.; Forte, E.; Areggi, G.; Mocnik, A.; Zini, L. Non-invasive methodological approach to detect and characterize high-risk sinkholes in urban cover evaporite karst: Integrated reflection seismics, PS-InSAR, leveling, 3D-GPR and ancillary data. A NE Italian case study. *Remote Sens.* **2020**, *12*, 3814. [CrossRef]

55. Parise, M. Sinkholes, subsidence and related mass movements. In *Treatise on Geomorphology 5*; Shroder, J.J.F., Ed.; Academic Press: Cambridge, MA, USA; Elsevier: Amsterdam, The Netherlands, 2022; pp. 200–220. [CrossRef]
56. Sevil, J.; Gutiérrez, F. Morphometry and evolution of sinkholes on the western shore of the Dead Sea. Implications for susceptibility assessment. *Geomorphology* **2023**, *434*, 108732. [CrossRef]
57. Gonçalves, J.A.; Henriques, R. UAV photogrammetry for topographic monitoring of coastal areas. *ISPRS J. Photogramm.* **2015**, *104*, 101–111. [CrossRef]
58. Turner, I.L.; Harley, M.D.; Drummond, C.D. UAVs for coastal surveying. *Coast Eng.* **2016**, *114*, 19–24. [CrossRef]
59. Carrivick, J.L.; Smith, M.W.; Quincey, D.J. *Structure from Motion in the Geosciences*; Collection of New Analytical Methods in Earth Environ Sci; John Wiley & Sons: Chichester, UK, 2016. [CrossRef]
60. Seong, K.; Leeb, T.; Singhc, V.P. UAV Photogrammetry-based Sea Level Establishment for a Storm Surge Early Warning System in Wolpo-beach, South Korea. *KSCE J. Civ. Eng.* **2024**, *28*, 2505–2514. [CrossRef]
61. Albuquerque, M.; Alves, D.C.L.; Espinoza, J.M.A.; Oliveira, U.R.; Simões, R.S. Determining shoreline response to meteo-oceanographic events using remote sensing and unmanned aerial vehicle (UAV): Case study in southern Brazil. *J. Coast Res.* **2018**, *85*, 766–770. [CrossRef]
62. Brunetta, R.; Duo, E.; Ciavola, P. Evaluating Short-Term Tidal Flat Evolution Through UAV Surveys: A Case Study in the Po Delta (Italy). *Remote Sens.* **2021**, *13*, 2322. [CrossRef]
63. Duo, E.; Trembanis, A.C.; Dohner, S.; Grottoli, E.; Ciavola, P. Local-scale post-event assessments with GPS and UAV-based quick-response surveys: A pilot case from the Emilia–Romagna (Italy) coast. *NHESS* **2018**, *18*, 2969–2989. [CrossRef]
64. Adams, S.M.; Friedlandb, C.J.; Levitanc, M.L. Unmanned Aerial Vehicle Data Acquisition for Damage Assessment in Hurricane Events. In Proceedings of the 8th International Workshop on Remote Sensing for Disaster Management, Tokyo, Japan, 30 September–1 October 2010.
65. Biolchi, S.; Furlani, S.; Devoto, S.; Scicchitano, G.; Korbar, T.; Vilibić, I.; Šepić, J. The origin and dynamics of coastal boulders in a semi-enclosed shallow basin: A northern Adriatic case study. *Mar. Geol.* **2019**, *411*, 62–77. [CrossRef]
66. Pinton, D.; Canestrelli, A.; Moon, R.; Wilkinson, B. Estimating Ground Elevation in Coastal Dunes from High-Resolution UAV-LIDAR Point Clouds and Photogrammetry. *Remote Sens.* **2023**, *15*, 226. [CrossRef]
67. Casella, E.; Drechsel, J.; Winter, C.; Benninghoff, M.; Rovere, A. Accuracy of sand beach topography surveying by drones and photogrammetry. *Geo-Mar. Lett.* **2020**, *40*, 255–268. [CrossRef]
68. Laporte-Fauret, Q.; Marieu, V.; Castelle, B.; Michalet, R.; Bujan, S.; Rosebery, D. Low-Cost UAV for High-Resolution and Large-Scale Coastal Dune Change Monitoring Using Photogrammetry. *J. Mar. Sci. Eng.* **2019**, *7*, 63. [CrossRef]
69. Mancini, F.; Dubbini, M.; Gattelli, M.; Stecchi, F.; Fabbri, S.; Gabbianelli, G. Using unmanned aerial vehicles (UAV) for high-resolution reconstruction of topography: The structure from motion approach on coastal environments. *Remote Sens.* **2013**, *5*, 6880–6898. [CrossRef]
70. Casagrande, G.; Bezzi, A.; Fracaros, S.; Martinucci, D.; Pillon, S.; Salvador, P.; Sponza, S.; Fontolan, G. Quantifying Transgressive Coastal Changes Using UAVs: Dune Migration, Overwash Recovery, and Barrier Flooding Assessment and Interferences with Human and Natural Assets. *J. Mar. Sci. Eng.* **2023**, *11*, 1044. [CrossRef]
71. Fontolan, G.; Bezzi, A.; Casagrande, G.; Fracaros, S.; Popesso, C.; Spadotto, S.; Favaro, M.; Papa, A. Real-Time Monitoring System and an Early Warning System Implemented. Report D 5.4.3_Part B_ Stream project 2023. Available online: https://programming14-20.italy-croatia.eu/web/stream/docs-and-tools-details?id=2136615&nAcc=5&file=12 (accessed on 23 April 2024).
72. Archivio di Stato di Trieste. Available online: https://archiviodistatotrieste.it/documento-del-mese/novembre-2023-mareggiate-a-trieste/ (accessed on 23 April 2024).
73. Zini, L.; Calligaris, C.; Cucchi, F. Along the hidden Timavo. *GFT&M* **2022**, *14*, 1–69. [CrossRef]
74. Jurkovšek, B.; Biolchi, S.; Furlani, S.; Kolar-Jurkovšek, T.; Zini, L.; Jež, J.; Tunis, G.; Bavec, M.; Cucchi, F. Geology of the Classical Karst Region (SW Slovenia–NE Italy). *J. Maps* **2016**, *12*, 352–362. [CrossRef]
75. Schmid, S.M.; Bernoulli, D.; Fügenschuh, B.; Matenco, L.; Schefer, S.; Schuster, R.; Tischler, M.; Ustaszewski, K. The Alpine-Carpathian-Dinaridic orogenic system: Correlation and evolution of tectonic units. *Swiss J. Geosci.* **2008**, *101*, 139–183. [CrossRef]
76. van Unen, M.; Matenco, L.; Nader, F.H.; Darnault, R.; Mandic, O.; Demir, V. Kinematics of foreland-vergent crustal accretion: Inferences from the Dinarides evolution. *Tectonics* **2019**, *38*, 49–76. [CrossRef]
77. van Hinsbergen, D.J.; Torsvik, T.H.; Schmid, S.M.; Maţenco, L.C.; Maffione, M.; Vissers, R.L.; Gürer, D.; Spakman, W. Orogenic architecture of the Mediterranean region and kinematic reconstruction of its tectonic evolution since the Triassic. *Gondwana Res.* **2020**, *81*, 79–229. [CrossRef]
78. Korbar, T. Orogenic evolution of the External Dinarides in the NE Adriatic region: A model constrained by tectonostratigraphy of Upper Cretaceous to Paleogene carbonates. *Earth-Sci. Rev.* **2009**, *96*, 296–312. [CrossRef]
79. Balling, P.; Tomljenović, B.; Schmid, S.M.; Ustaszewski, K. Contrasting along-strike deformation styles in the central external Dinarides assessed by balanced cross-sections: Implications for the tectonic evolution of its Paleogene flexural foreland basin system. *Global Planet Change* **2021**, *205*, 103587. [CrossRef]
80. Consorti, L.; Corradetti, A.; Hadi, M.; Franceschi, M.; Sabbatino, M.; Bensi, S.; Bertone, N.; Bonini, L. Biostratigraphic investigations assisted by virtual outcrop modeling: A case study from an Eocene shallow-water carbonate succession (Val Rosandra gorge, Trieste, NE Italy). *Ital. J. Geosci.* **2024**, *143*, 60–74. [CrossRef]

81. Zini, L.; Calligaris, C.; Forte, E.; Turpaud, P. Flood hazard assessment in a polje: The case of Mucille (Classical Karst Region, NE Italy). *Environ. Earth Sci.* **2023**, *82*, 293. [CrossRef]
82. Furlani, S.; Ninfo, A.; Zavagno, E.; Paganini, P.; Zini, L.; Biolchi, S.; Antonioli, F.; Coren, F.; Cucchi, F. Submerged notches in Istria and The Gulf of Trieste: Results from the Geoswim Project. *Quat. Int.* **2014**, *332*, 37–47. [CrossRef]
83. Trobec, A.; Busetti, M.; Zgur, F.; Baradello, L.; Babich, A.; Cova, A.; Gordini, E.; Romeo, R.; Tomini, I.; Poglajen, S.; et al. Thickness of marine Holocene sediment in the Gulf of Trieste (northern Adriatic Sea). *Earth Syst. Sci. Data* **2018**, *10*, 1077–1092. [CrossRef]
84. Bezzi, A.; Casagrande, G.; Fracaros, S.; Martinucci, D.; Pillon, S.; Sponza, S.; Bratus, A.; Fattor, F.; Fontolan, G. Geomorphological changes of a migrating sandbank: Multidecadal analysis as a tool for managing conflicts in coastal use. *Water* **2021**, *13*, 3416. [CrossRef]
85. Brambati, A. Modificazioni costiere nell'arco lagunare dell'Adriatico Settentrionale. *Antich. Altoadriatiche* **1985**, *27*, 13–47.
86. Marocco, R. Lineamenti geomorfologici della costa e dei fondali del Golfo di Trieste e considerazioni sulla loro evoluzione tardo-quaternaria. *Int. J. Speleol.* **1989**, *18*, 87–110. [CrossRef]
87. Gordini, E.; Caressa, S.; Marocco, R. Nuova carta morfo-sedimentologica del Golfo di Trieste (Da Punta Tagliamento alla foce dell'Isonzo). *Gortania. Atti. Mus. Friul. Stor. Nat.* **2003**, *25*, 5–29.
88. European Marine Observation and Data Network (EMODnet). Available online: http://www.emodnet-bathymetry.eu (accessed on 10 June 2024).
89. Trobec, A.; Busetti, M. Models of the bathymetry, of the base and of the thickness of Holocene marine sediment in the Gulf of Trieste (Northern Adriatic Sea). *OGS SNAP System*. 2017. Available online: https://snap.ogs.it/cache/doi/6ad9b1e6-c977-cec9-8a2d-db10c7f90adc/58074ea270863f0a32214fab4f43d42c.jsp (accessed on 10 June 2024).
90. Petti, M.; Pascolo, S.; Bosa, S.; Bezzi, A.; Fontolan, G. Tidal Flats Morphodynamics: A new Conceptual Model to Predict Their Evolution over a Medium-Long Period. *Water* **2019**, *11*, 1176. [CrossRef]
91. Dorigo, L. La Laguna di Grado e le Sue Foci. Ricerche e Rilievi Idrografici. *Magistr. Alle Acque-Ufficio Idrografico* **1965**, *155*, 1–231.
92. RAFVG. Piano Regolatore Portuale del Porto di Monfalcone, Variante Localizzata. Studio Meteomarino. 2019. Available online: https://www.regione.fvg.it/rafvg/export/sites/default/RAFVG/ambiente-territorio/pianificazione-gestione-territorio/FOGLIA9/allegati/Allegato_33_alla_Delibera_2066-2019.pdf (accessed on 23 April 2024).
93. Triestenews. Available online: https://www.triesteallnews.it/2023/11/uno-spettacolo-di-desolazione-la-mareggiata-che-travolse-trieste-nel-1911/ (accessed on 23 April 2024).
94. Il Piccolo. Available online: https://ilpiccolo.gelocal.it/trieste/cronaca/2023/11/13/news/mareggiata_trieste_danni_quattro_milioni-13856672/ (accessed on 25 September 2024).
95. Amoudry, L.O.; Souza, A.J. Deterministic coastal morphological and sediment transport modeling: A review and discussion. *Rev. Geophys.* **2011**, *49*. [CrossRef]
96. Baldoni, A.; Melito, L.; Marini, F.; Galassi, G.; Giacomin, P.; Filomena, G.; Barbizzi, N.; Lorenzoni, C.; Brocchini, M. Modeling coastal inundation for adaptation to climate change at local scale: The case of Marche Region (central Italy). *Front. Clim.* **2024**, *6*, 1334625. [CrossRef]
97. Chaumillon, E.; Bertin, X.; Fortunato, A.B.; Bajo, M.; Schneider, J.L.; Dezileau, L.; Walsh, J.P.; Michelot, A.; Chauveau, E.; Créach, A.; et al. Storm-induced marine flooding: Lessons from a multidisciplinary approach. *Earth-Sci. Rev.* **2017**, *165*, 151–184. [CrossRef]
98. Chen, Z.; Luo, F.; Zhou, G.; Zhu, F.; Wu, H.; Li, R.; Zhang, C. Hydrodynamic modeling study of nature-based hybrid coastal defense strategy applied in salt marsh restoration. *Estuar. Coast Shelf Sci.* **2024**, *298*, 108666. [CrossRef]
99. Yaiche Temam, I.; Bouhmadouche, M.; Hemdane, Y.; Kessali, N.; Amiri, H. Analysis of the hydrosedimentary circulation in the mouth of dominated wave environment using grain size analysis, wave/current modeling and image processing case of the principal Rivers in Zemmouri bay. *MESE* **2024**, *10*, 4279–4294. [CrossRef]
100. Verhoeven, G. Taking computer vision Aloft-archaeological three-dimensional reconstructions from aerial photographs with photoscan. *Archaeol. Prospect* **2011**, *18*, 67–73. [CrossRef]
101. Ullman, S. The interpretation of structure from motion. *Proc. R Soc. Lond. B* **1979**, *203*, 405–426. [CrossRef] [PubMed]
102. Grün, A.; Remondino, F.; Zhang, L. Photogrammetric reconstruction of the Great Buddha of Bamiyan, Afghanistan. *Photogramm. Rec.* **2004**, *19*, 177–199. [CrossRef]
103. Szeliski, R. Image processing. In *Computer Vision: Algorithms and Applications*; Springer: Cham, Switzerland, 2022; pp. 85–151. [CrossRef]
104. Vaccher, V.; Hastewell, L.; Devoto, S.; Corradetti, A.; Mantovani, M.; Korbar, T.; Furlani, S. The application of UAV-derived SfM-MVS photogrammetry for the investigation of storm wave boulder deposits on a small rocky island in the semi-enclosed Northern Adriatic Sea. *Geomat. Nat. Haz. Risk* **2024**, *15*, 2295817. [CrossRef]
105. Seitz, S.M.; Curless, B.; Diebel, J.; Scharstein, D.; Szeliski, R. A comparison and evaluation of multi-view stereo reconstruction algorithms. In Proceedings of the 2006 IEEE Computer Society Conference on Computer Vision and Pattern Recognition—Volume 1 (CVPR'06), New York, NY, USA, 5 June 2006; pp. 519–528. [CrossRef]
106. Corradetti, A.; Seers, T.; Mercuri, M.; Calligaris, C.; Busetti, A.; Zini, L. Benchmarking Different SfM-MVS Photogrammetric and iOS LiDAR Acquisition Methods for the Digital Preservation of a Short-Lived Excavation: A Case Study from an Area of Sinkhole Related Subsidence. *Remote Sens.* **2022**, *14*, 5187. [CrossRef]

107. CloudCompare: 3D Point Cloud and Mesh Processing Software Open Source Project. Available online: https://www.danielgm.net/cc/ (accessed on 10 June 2024).
108. Kim, H.; Kim, H.; Hyun, C.-U.; Park, H.-D.; Cha, J. Image Mapping Accuracy Evaluation Using UAV with Standalone, Differential (RTK), and PPP GNSS Positioning Techniques in an Abandoned Mine Site. *Sensors* **2023**, *23*, 5858. [CrossRef]
109. Tavani, S.; Pignalosa, A.; Corradetti, A.; Mercuri, M.; Smeraglia, L.; Riccardi, U.; Seers, T.; Pavlis, T.; Billi, A. Photogrammetric 3D Model via Smartphone GNSS Sensor: Workflow, Error Estimate, and Best Practices. *Remote Sens.* **2020**, *12*, 3616. [CrossRef]
110. Corradetti, A.; Seers, T.D.; Billi, A.; Tavani, S. Virtual Outcrops in a Pocket: The Smartphone as a Fully Equipped Photogrammetric Data Acquisition Tool. *GSA Today* **2021**, *31*, 4–9. [CrossRef]